Article

Evapotranspiration Estimation with UAVs in Agriculture: A Review

Haoyu Niu [1,†,*], Tiebiao Zhao [1], Dong Wang [2] and YangQuan Chen [1]

1 University of California, Merced; hniu2@ucmerced.edu
2 USDA-ARS Water Management Research Unit, San Joaquin Valley Agricultural Sciences Center, Parlier, California, USA, 93648
* Correspondence: hniu2@ucmerced.edu; Tel.: +1-530-566-6577
† Current address: Room 22, 4225 Hospital Road, Atwater, California, 95301, USA

Abstract: Estimating evapotranspiration (ET) has been one of the most important research in agriculture recently because of water scarcity, growing population, and climate change. ET is the sum of evaporation from the soil and transpiration from the crops to the atmosphere. The accurate estimation and mapping of ET are necessary for crop water management. Traditionally, people use weighing lysimeters, Bowen ratio, eddy covariance and many other methods to estimate ET. However, these ET methods are points or location-specific measurements and cannot be extended to a large scale of ET estimation. With the advent of satellites technology, remote sensing images can provide spatially distributed measurements. The satellites multispectral images spatial resolution, however, is in the range of meters, which is often not enough for crops with clumped canopy structure such as trees and vines. And, the timing or frequency of satellites overpass is not always enough to meet the research or water management needs. The Unmanned Aerial Vehicles (UAVs), commonly referred to as drones, can help solve these spatial and temporal challenges. Lightweight cameras and sensors can be mounted on drones and take high-resolution images on a large scale of field. Compared with satellites images, the spatial resolution of UAVs' images can be as high as 1 cm per pixel. And, people can fly a drone at any time if the weather condition is good. Cloud cover is less of a concern than satellite remote sensing. Both temporal and spatial resolution is highly improved by drones. In this paper, a review of different UAVs based approaches of ET estimations are presented. Different modified models used by UAVs, such as Mapping Evapotranspiration at high Resolution with Internalized Calibration (METRIC), Two-source energy balance (TSEB) model, etc, are also discussed.

Keywords: Clumped canopy; evapotranspiration; Unmanned aerial vehicles; METRIC; remote sensing;

---

1. Introduction

Evapotranspiration (ET) estimation is important in precision agriculture water management. ET is known as the main outgoing water flux from the surface on the earth [1]. Mapping the ET temporally and spatially can be useful for evaluating soil moisture [2], drought monitoring [3], assessing crop water stress [4], etc. It is important to accurately quantify the ET in order to get a better understanding of crop growth. Estimating the ET accurately can also benefit the water resources management and weather forecast [5]. ET is a combination of two separate processes, the evaporation and the transpiration. Evaporation is the process whereby liquid water is converted to water vapour [6]. Then, the water vapour removes from the evaporating surface. Transpiration is the process of the vaporization of liquid water contained in plant tissues and the vapour removal to the atmosphere [6]. The current theory for transpiration is by the following three steps. First, the conversion of liquid phase water to vapor water, the side effect is to cause canopy cooling from latent heat exchange thus canopy temperature can be used as an indicator of ET. Second, diffusion of water molecules from

Preprints (www.preprints.org) | NOT PEER-REVIEWED | Posted: 8 July 2019 doi:10.20944/preprints201907.0124.v1

inside plant stomata on the leaves to the surrounding atmosphere. Third, atmospheric air mixing by convection or diffusion can transport vapor near the plant surfaces to the upper atmosphere or off site away from the plant canopy. Usually, evaporation and transpiration occur simultaneously.

To estimate ET, there are direct and indirect methods. For direct methods, there are lysimeters [7] and water balance methods [8]

$$WB = P + I - D - R - S = ET, \tag{1}$$

where WB (mm day^{-1}) is water balance and P (mm day^{-1}) means precipitation. I (mm day^{-1}) is irrigation, D (mm day^{-1}) means drainage, R (mm day^{-1}) is runoff. S (mm day^{-1}) is the soil moisture storage. ET (mm day^{-1}) is the evapotranspiration of the plant. However, these ET methods are usually point or location-specific measurements and cannot be extended to a large scale of ET estimation because of the heterogeneity of the land surface. And, the hydrologic processes can be very complex, too. Researchers sometimes also need to get variable land surface measurements and parameters [9], which is unlikely to get by these traditional methods. The experiment equipment is also very expensive, such as lysimeter, which is only available for a small group of people.

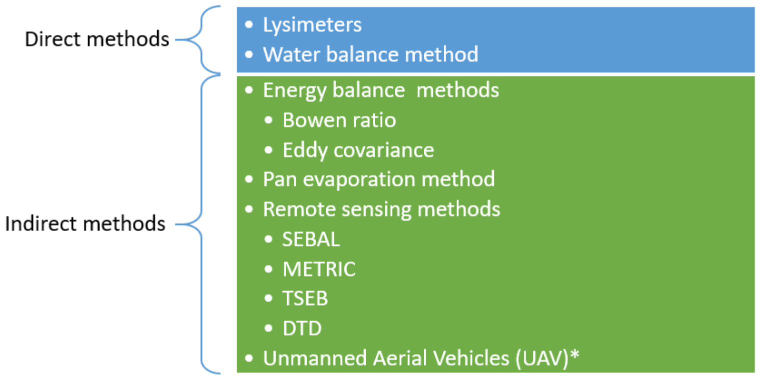

Figure 1. The direct and indirect methods for ET estimation

For indirect methods, there are energy balance methods [1], Pan evaporation methods [8] [10], and remote sensing methods [11]. For energy balance methods, Bowen ratio [12] [13] and eddy covariance [14] have been widely used in ET estimation. Over the past decades, remote sensing techniques have been considered as one of the most powerful methods for mapping and estimating ET [15] [16]. Because they can detect variations in vegetation and soil condition over space and time, remote sensing energy balance models have been useful to account for the spatial variability of ET at regional scales when using satellite platforms such as Landsat and ASTER [17] [18] [19] [20] [21]. Related research has been reviewed a few times [22] [23] [24]. Remote sensing techniques can provide information about Normalized Difference Vegetation Index (NDVI), Leaf Area index (LAI), surface temperature, surface albedo and so on. Several remote sensing models have been developed over the past decades, such as Surface Energy Balance Algorithm for Land (SEBAL) [18] [11], Mapping Evapotranspiration with Internalized Calibration (METRIC) [25], the Dual Temperature Difference (DTD) [26], and the Priestley-Taylor TSEB (TSEB-PT) [27]. There are mainly four energy fluxes in these remote sensing energy balance models, which are net radiation R_n, soil heat flux G, latent heat flux LE and sensible heat flux H. Satellites images can help researchers get spatially distributed measurements, though, the resolution for those images are usually 30 m, which are not good enough for many precision agriculture or ecological applications. Second, the timing of satellites overpass is not always synchronous with research requirements, they usually have a two-week revisit cycle [28]. Third, obtaining high-resolution images can be very expensive [21]. All these disadvantages limit the ET estimation by using traditional satellites images.

Preprints (www.preprints.org) | NOT PEER-REVIEWED | Posted: 8 July 2019 doi:10.20944/preprints201907.0124.v1

As a new potential remote sensing platform, researchers are more and more interested in the potential of UAV data not only in precision agriculture, but also in different scientific and commercial communities [29] [30] [31] [32]. Drones can overcome some of those remote sensing limitations. For example, satellite remote sensing is prone to cloud cover, drones are below the clouds. Compared with satellites, UAVs can be operated at any time if the weather is good. Satellite has fixed flight path, drones are more mobile and more adaptive for site selection. And most drones are cost-effective (thousands of dollars). Mounted on the UAVs, light weight sensors, such as RGB cameras, multispectral cameras, and thermal infrared cameras, can help get higher resolution images. And, higher resolution images are important for recognizing the temporal and spatial variability related to the crops. UAVs have already been widely and successfully used in other agriculture research, such as water stress [33], tree canopy segmentation [34], counting watermelons [35]. Therefore, UAVs have great potential to help estimate ET. Many researchers have already been using UAVs for ET estimation. For example, in [36], the author implemented a remote sensing energy balance (RSEB) algorithms for estimating energy components, such as incoming solar radiation, sensible heat flux, soil heat flux and latent heat flux. Optical sensors were mounted on a UAV to provide high spatial resolution images. By using the UAV platform, experiments results show that the RSEB algorithm can estimate latent heat flux and sensible heat flux with errors of 7% and 5% respectively. It demonstrates that UAV could be used as an excellent platform to evaluate spatial variability in the field.

The rest of the paper is organized as follows. Section II introduces different UAV types being used for ET estimation. Advantages and disadvantages are discussed for them. Several commonly used light weight sensors are also compared in this section. UAV path planning and image processing methods are presented in the second section, too. In section III, the ET estimation methods and models for UAVs agricultural application, such as Two source energy balance (TSEB) model and METRIC model, are discussed. In Section IV, different results of ET estimation methods and models are compared and discussed. Challenges and opportunities for UAVs are mentioned in the conclusion section.

2. Materials and Methods

2.1. Unmanned aerial vehicles (UAV) and light weight sensors

Many kinds of unmanned aerial vehicles are used on different research purposes for ET estimation. Typically, there are two different UAV platforms, fixed-wings, and quadcopter. Fixed-wings can usually fly longer and carry heavy sensors. It can usually fly about 2 hours, which is suitable for a large scale of field. Quadcopters can fly about 30 minutes, which is used for short flight mission in a small scale of field.

In [27], researchers used a fixed-wing UAV to collect thermal data to estimate ET with two source energy balance models. The drone has a 2.2-meter wing span, which can fly 25 minutes when carrying a 2-kilogram payload. The drone was flying at a height of 90 meters with a speed of 60 km/h, which could cover a 400 m $\times$ 400 m area in one flight. The SkyCircuits ground control station is used to design the flight path and for flight inspection. To collect thermal data, they used an Optris PI 450 LW infrared camera. Based on the specifications, this uncooled thermal camera has an accuracy of ± 2 °C or ± 2 % when the ambient temperature is between 0 °C to 70 °C. The thermal images have a spectral range of 7.9 μm and and an optical resolution of 382 $\times$ 288 pixels.

In [37], multispectral and thermal images were collected by using an airborne digital system developed by Utah State University. The digital system was installed in a Cessna TU206 aircraft, which also has four ImperX Bobcat B8430 digital cameras. The spectral bands for these cameras are, Red (0.645 μm - 0.655 μm), Green (0.545 μm – 0.555 μm), Blue (0.465 μm – 0.475 μm) and Near-infrared (NIR) (0.780 μm – 0.820 μm). A ThermalCAM SC640 (FLIR Systems Inc.) is also mounted on the aircraft to collect thermal infrared (TIR) images, the wavelength range is 7.5 μm – 13 μm.

In [21], the author estimated evapotranspiration in a peach orchard by using very-high-resolution imagery from an UAV platform (S1000, DJI, Shenzhen, China). A TIR camera (A65, FLIR Systems Inc.)

and a multispectral camera RedEdge M (MicaSense, Seattle, WA, USA) are also mounted on the drone. The thermal camera A65 has a spatial resolution of 640 × 512 pixels. It has a Field of View (FOV) of 25° (H) × 20° (V). The focal length for this TIR camera is 25 mm. For the RedEdge, it has five different bands, Red (668 nm), Green (560 nm), Blue (475 nm), Red edge (717 nm) and Near-infrared (840 nm). RedEdge M has spatial resolution of 1280 × 960 pixels with a focal length of 5.5 nm.

Quadcopters have been widely used in agricultural research, such as [34] [38], which promises a great potential in ET estimation. In [34], a quadcopter named Hover was used as the UAV platform to collect aerial images, as shown in Figure 2.

Figure 2. The Hover is equipped with a Pixhawk flight controller, GPS, telemetry antennas. Its lithium polymer battery has a capacity of 9500 mAh, which can support a 30-minute flight mission with a camera mounted on it.

The Hover was equipped with a Pixhawk flight controller, GPS, telemetry antennas. And, it can fly over the field by waypoints mode (designed by using Mission Planner software). The Hover's lithium polymer battery has a capacity of 9500 mAh, which can support a 30-minute flight mission with cameras mounted on the Hover drone.

To estimate ET, multispectral images can be collected by Survey 2 (MAPIR, USA) cameras with 4 bands, Blue, Green, Red (RGB) and Near-infrared (NIR). The MAPIR camera has a resolution of 4608 × 3456 pixels, with a space resolution at 1.01 cm/pixel. The Survey 2 cameras have a faster interval timer, 2 seconds for JPG mode and 3 seconds for RAW + JPG mode. Faster interval timer would benefit the overlap design for UAV flight missions, such as reducing the flight time, enabling higher overlapping. Another multispectral camera being used is Rededge M (MicaSense, USA). The Rededge M has five bands, which are Blue, Green, Red, Near infrared, and Red edge. It has a resolution of 1280 × 960 pixel, with a 46° field of view. With a Downwelling Light Sensor (DLS), which is a 5-band light sensor that connects to the camera, the Rededge M can measure the ambient light during a flight mission for each of the five bands. Then it can record the light information in the metadata of the images captured by the camera. After the camera calibration, the information detected by the DLS can be used to correct lighting changes during a flight, which usually happens because the clouds cover the sun during a UAV flight.

The thermal camera ICI 9640 P-Series (ICI, USA) was applied for collecting thermal images. The thermal camera has a resolution of 640 × 480 pixels. The spectral band is from 7 μm to 14 μm. The dimension of the thermal camera is 34 mm × 30 mm × 34 mm. The accuracy is supposed to be ± 2 °C. A Raspberry Pi Model B computer was used to trigger the thermal cameras during the flight missions. The SWIR 640 P-Series, which is a shortwave infrared camera, can also be used for ET estimation. The spectral band is from 0.9 μm to 1.7 μm. The accuracy for SWIR camera is ± 1 °C. It has a resolution of 640 × 512 pixels.

Preprints (www.preprints.org) | NOT PEER-REVIEWED | Posted: 8 July 2019 doi:10.20944/preprints201907.0124.v1

Table 1. Some commonly used sensors on UAV platforms.

Sensors	Function	Resolution	Accuracy
Rededge M	Multispectral	1280 × 960 pixels	8.2 cm/pixel (per band) at 120 m
MAPIR Survey 2	Multispectral	4608 × 3456 pixels	4.05 cm/pixel at 120 m
Mini MCA-6	Multispectral	1280 × 1024 pixels	3.3 cm/pixel at 60 m
Sequoia	Multispectral	4608 × 3456 pixels	17 cm/pixel at 100 m
Cannon S 110	Near infrared	4000 × 3000 pixels	3.5 cm/pixel at 100 m
ICI 9640 P	Thermal infrared	640 × 480 pixel	±1 °C
ICI SWIR 640 P	Short-wave infrared	640 × 512 pixel	±1 °C
Optris PI 450	Thermal infrared	382 ×288 pixels	±2 °C or ±2 %
ThermalCAM SC640	Thermal infrared	640 × 480 pixel	±2 °C or ±2 %
EasIR-9	Thermal infrared	288 × 384 pixel	±2 °C or ±2 %
thermoMAP	Thermal infrared	640 × 512 pixel	14 cm/pixel at 75 m

Some commonly used sensors are listed in the Table 1 for comparison. Compared with traditional remote sensing method, such as satellites, the thermal camera and UAVs make the data collection more flexible and lower cost. Thermal remote sensing images were first used in 1973 to estimate ET [39]. Temperature information is usually converted into land surface characteristics such as albedo, LAI, and surface emissivity. The TIR band is considered as the most important variable because it plays an important role in sensible heat flux and ground heat flux [40]. The cooled thermal cameras are usually more sensitive and accurate than uncooled thermal cameras [41]. But cooled thermal cameras are very big, expensive, and energy consuming [42]. So, they can hardly be used on UAV platform. In contrast, the uncooled thermal camera plays a more and more important role because they are light [43], low power consumption [44] and less expensive than cooled thermal cameras. As mentioned previously, uncooled thermal cameras have been widely used in UAV platform for ET estimation. Not only for ET, it also has been widely used in many other agricultural applications, such as plant disease detection [45], crop water stress estimation [46] [47] and soil moisture detection [48]. And most importantly, they can measure two of the most important parameters of ET estimation, soil temperature and tree canopy temperature, which are widely used in two source energy balance models, SEBAL, and METRIC.

The thermal camera has so many advantages, though, its micobolometer is not always sensitive and accurate [42]. Also, most thermal cameras are not always calibrated, which can only measure the relative temperature instead of the accurate value. In precision agriculture, however, most time it's necessary to measure the accurate temperature in many applications [43] such as crop monitoring [49], pest detection [50] and disease detection [45]. Unstable outdoor environmental factors can cause serious measurement drift during flight missions. Post-processing like mosaicking might further lead to measurement errors. We are using thermal camera more and more frequently with its limitations. To answer these two fundamental questions, in [51], the authors finished three experiments to research the best practice of thermal images collection for UAV. To calibrate TIR images, in [21], they used water body and rubber plates as cold and hot features. IR Flash Version 2 is usually used to process thermal UAV images for image format transformation.

2.2. UAV path planning and image processing

In this section, we discussed the potential of path planning and image processing methods for ET estimation. Recently, unmanned aerial vehicles have been widely used in agriculture, such as crop yield estimation [35], soil moisture monitoring, water stress estimation [33] and pest management [52]. Compared with traditional remote sensing tools, such as satellites, drones' flight time can be more flexible and more frequent in the field. And, drones can fly at lower altitude and can take higher spatial and possibly temporal resolution images and thermal images [51] of crops. As a low-cost scientific data collection platform, drones also make data acquisition relatively less expensive. While there are many advantages by using drones for agricultural applications [35], there is still a lot of work for drones when used for estimating evapotranspiration. Many researchers fly the drones in different height,

Preprints (www.preprints.org) | NOT PEER-REVIEWED | Posted: 8 July 2019 doi:10.20944/preprints201907.0124.v1

using specialized equipment, controlling environments and relying on data analysis expertise [53]. Is there any optimal point where the data can be the best representation of crops? In [53], Brandon built a conceptual framework for describing the optimality as a function of spatial, spectral, and temporal factors which represent the best solution. As researchers try to understand the potential of the UAVs, efficient workflow, image processing methods, and better software are still under developing [54] [55] [56] [57].

2.2.1. Pre-flight path planning

Being used as a remote sensing platform, UAVs also create new research problems, such as drone image processing, and flight path planning. Flight missions were programmed by using Mission Planner software. The flight height was setup as 30 m, 60 m, and 120 m in order to compare the image resolution's effect on pomegranate ET estimation. For all the flight missions, the overlap was set up as 75% to make sure the images can be stitched together during images pre-processing. The UAV sensors are designed to take images at nearly 0 nadir angle.

Researchers usually fly drones biweekly to collect data. If there is a drone crash, hardware issues, or unknown reasons, data may not be collected successfully. And, there is only one growing season each year. If data is missed, people have to wait for another year. In order to get enough data, for our research, we flew the drone Hover bi-weekly over the pomegranate field at noon during the growing season in 2017 and 2018. Table 2 is an example of data collection in 2018 by using Survey 2 (MAPIR, USA) and ICI 9460 P (ICI, USA) thermal camera.

Table 2. Multispectral and thermal images collection by UAV during the 2018 growing season at Parlier, CA, USA. -* means there is no data for that day.

Date	Flight time	MAPIR Survey 2	ICI 9460P
4-12-18	12 - 2 pm	30, 60, 120 m	30 m
4-26-18	12 - 2 pm	30, 60, 120 m	30 m
5-9-18	12 - 2 pm	30, 60, 120 m	30 m
5-23-18	12 - 2 pm	30, 60, 120 m	30 m
6-8-18	12 - 2 pm	30, 60, 120 m	-*
6-13-18	12 - 2 pm	30, 60, 120 m	30 m
6-28-18	12 - 2 pm	30, 60, 120 m	-*
7-11-18	12 - 2 pm	30, 60, 120 m	-*
7-25-18	12 - 2 pm	30, 60, 120 m	30 m
8-8-18	12 - 2 pm	30, 60, 120 m	30 m
8-22-18	12 - 2 pm	30, 60, 120 m	30 m
9-14-18	12 - 2 pm	30, 60, 120 m	30 m
10-9-18	12 - 2 pm	30, 60, 120 m	30 m
10-16-18	12 - 2 pm	30, 60, 120 m	30 m
10-30-18	12 - 2 pm	30, 60, 120 m	30 m

2.2.2. Image calibration

In order to minimize the shading effect on the images, the drones are usually flying at noon with clear sky conditions. And, because each pixel in a drone image is a percentage of the reflected light, we need to calibrate the pixel value by using a known reflectance value. Therefore, the images of a color panel were taken right before and after the flight missions, servicing as the reflectance reference.

 doi:10.20944/preprints201907.0124.v1

Figure 3. The images of a color panel were taken right before and after the flight missions, servicing as the reflectance reference.

It is important to take pictures of the reference panel immediately before and after the flight missions, because the solar angle and light intensity can change a lot based on an experiment in [47], which can cause inaccurate experiment results. Then, the digital number of the images were converted to reflectance by an empirical method in [58]

$$\rho_\lambda = \frac{DN - DN_d}{DN_w - DN_d}, \tag{2}$$

where ρ_λ is the reflectance and DN is the digital number of the raw image. DN_d and DN_w are the dark relflectance point and white reflectance point in color checker respectively.

2.2.3. Images stitching and orthomosaic image generation

After the flight missions, all of the aerial images were stitched together to generate the orthomosaick images in PhotoScan (Agisoft LLC, Russian). As shown in Table 3, there are usually three steps for image processing, which includes aligning photos, building mesh (optional) and generating orthomosaick. For example, the Agisoft Photoscan settings and workflow for RGB and NIR images (by MAPIR Survey 2) are listed in Table 3.

Table 3. Orthomosaic images generation workflow in Agisoft Photoscan

Step 1 : Align Photos	**Step 2 : Build Mesh**	**Step 3 : Build Orthomosaick**
Accuracy: Medium Generic preselection: Yes Key point limit: 40,000 Tie point limit: 4,000 Adaptive camera model fitting: No	Surface type: Height field (2.5D) Source data: Sparse cloud Face count: Medium (30,000) Interpolation: Enabled (default) Point classes: All Caculate vertex colors: Yes	Type: Planar Projection plane: TOP XY Rotation angle: 0 Surface: Mesh Blending mode: Mosaic (default) Enable hole filling: Yes Enable back-face culling: No

Preprints (www.preprints.org) | NOT PEER-REVIEWED | Posted: 8 July 2019 doi:10.20944/preprints201907.0124.v1

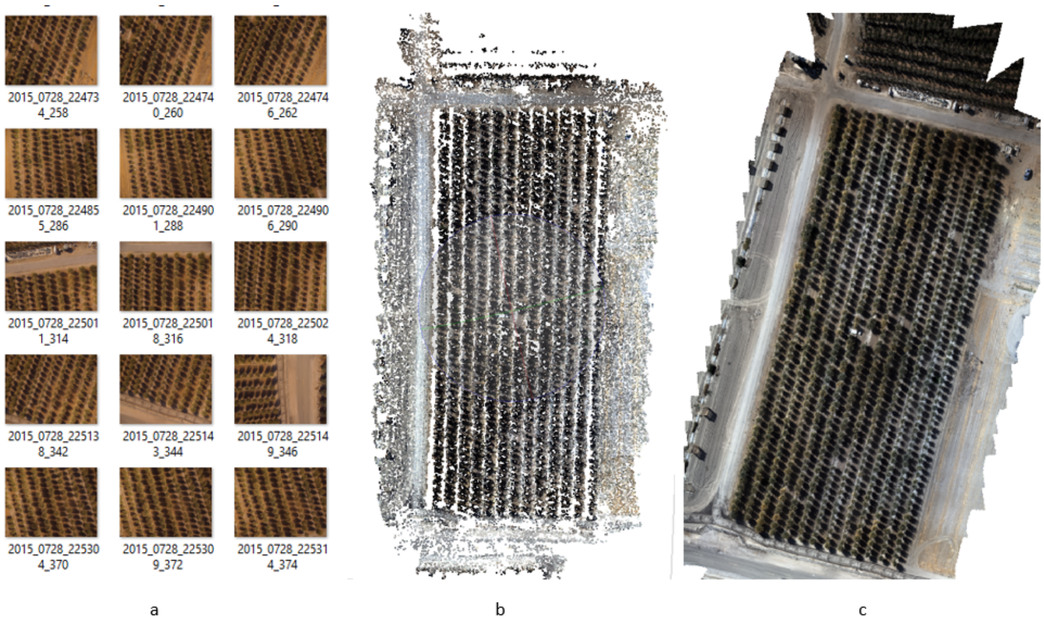

Figure 4. This is a image processing workflow to generate orthomosaick image for a pomegranate field (**a**) Some drone image examples taken by MAPIR . (**b**) Tie points images generated by Photoscan. (**c**) The orthomosaick image for the pomegranate field.

2.2.4. Post-processing calibrated images

In this subsection, a MATLAB code was written in order to calculate the normalized difference vegetation index (NDVI) by using the orthomosaick image. Many studies have used NDVI from remote sensing platform to help estimate crop coefficient values on crops, such as [59] [60] [61]. Then, crop coefficient can be applied to creating local and regional crop evapotranspiration (ET_c) maps. In [62] [63], they used a direct method to estimate ET by using the correlation between the ET, the remote sensing data, and the meteorological data. It is based on the assumption that daily ET has a correlation with the surface and air temperature. According to the relationship between NDVI and surface temperature, [64] [65] proposed a new direct method, which shows that NDVI and surface temperature have effect on the ET quantity. The relationship between the NDVI and surface temperature is strong, though, it changes by seasons [65]. LAI and fractional vegetation cover are also often calculated by using NDVI according to an empirical LAI-NDVI relation [66] [67].

Therefore, it is important to get NDVI values first before proceeding to further ET research. To calculate the NDVI, the following equation is used:

$$NDVI = \frac{\rho_{NIR} - \rho_R}{\rho_{NIR} + \rho_R}, \tag{3}$$

where ρ_{NIR} and ρ_R are the reflectance of near-infrared and red wavebands, respectively. After generating the NDVI image, QGIS was used to generate the pseudocolor map for the NDVI map, as shown in Figure 5.

Preprints (www.preprints.org) | NOT PEER-REVIEWED | Posted: 8 July 2019 doi:10.20944/preprints201907.0124.v1

Figure 5. NDVI map for a pomegranate field at USDA

3. ET Estimation Methods for UAV

Most ET estimation methods for UAVs are based on satellites remote sensing methods, the most widely used is energy balance models. TSEB, TSEB-PT, and DTD are introduced in this section. METRIC is also mentioned because of its potential in UAVs application. Researchers need to preprocess the images to input them in the METRIC model, because this model is originally for satellites images. But some research still shows good results [68].

3.1. Two source energy balance (TSEB) models

The TSEB is proposed by Norman [26] and modified by Norman and Kustas to improve the accuracy of LE estimation [24] [69] [70]. Based on [71] [72], the TSEB is effective over homogeneous land and environmental conditions. And, it can reproduce fluxes with similar results to tower-based observations. The TSEB model separates the land surface temperature into soil surface temperature and vegetation surface temperature, and it considers sensible and latent heat fluxes are transferred to the atmosphere from both surface temperature components, as shown in the following equations [37].

$$R_n = R_{ns} + R_{nc} = H + LE + G, \tag{4}$$

$$R_{ns} = H_s + LE_s + G, \tag{5}$$

$$R_{nc} = H_c + LE_c, \tag{6}$$

Preprints (www.preprints.org) | NOT PEER-REVIEWED | Posted: 8 July 2019 doi:10.20944/preprints201907.0124.v1

where R_n is the net radiation (W m^{-2}). The soil net radiation (W m^{-2}) is represented by R_{ns} and R_{nc} is the canopy net radiation (W m^{-2}). H is the sensible heat flux (W m^{-2}). H_s and H_c are soil sensible heat flux (W m^{-2}) and canopy sensible heat flux (W m^{-2}) respectively. LE is the latent heat flux (W m^{-2}). LE_s and LE_c are soil latent heat flux (W m^{-2}) and canopy latent heat flux (W m^{-2}) respectively. G is the soil heat flux (W m^{-2}).

$$H_s = \rho C_p \frac{T_s - T_{ac}}{R_s}, \tag{7}$$

$$H_c = \rho C_p \frac{T_c - T_{ac}}{R_x}, \tag{8}$$

where ρ is the air density (kg m^{-3}), C_p is the specific heat of air (J kg^{-1} K^{-1}). T_{ac} is the air temperature in the vegetation. R_s is the resistance to heat flux above the soil surface (s m^{-1}). R_x is the boundary layer resistance of the canopy leaves (s m^{-1}).

The net radiation is divided into two parts, the soil net radiation and the canopy net radiation [73] [74].

$$R_{ns} = \tau_l L_d + (1 - \tau_l)\varepsilon_c \sigma T_c^4 - \varepsilon_s \sigma T_s^4 + \tau_s (1 - \alpha_s) S_d, \tag{9}$$

$$R_{nc} = (1 - \tau_l)(L_d + \varepsilon_s \sigma T_s^4 - 2\varepsilon_c \sigma T_c^4) + (1 - \tau_s)(1 - \alpha_c) S_d, \tag{10}$$

where τ_l and τ_s are the longwave and shortwave radiation transmittances through the canopy. L_d and S_d are the incoming longwave and shortwave radiation (W m^{-2}), which are usually measured from a nearby weather station. σ is the Stefan-Boltzmann constant, which is approximately 5.67$\times$10^{-8} (W m^{-2} K^{-4}). ε is the surface emissivity. α is the surface albedo. And T is the surface temperature (K). Subscripts "s" and "c" mean soil and canopy.

In the TSEB model, the land surface temperature $T_R(\theta)$ is related to the soil and canopy component temperatures. The fraction of vegetation cover viewing angle θ also has effect on the estimation of $T_R(\theta)$, as shown in the following equation

$$T_R \approx [f_c(\theta) T_c^4 + (1 - f_c(\theta)) T_s^4]^{\frac{1}{4}}, \tag{11}$$

where $f_c(\theta)$ is the fractional vegetation cover observed as angle θ by radiometer. To calculate $f_c(\theta)$, the following equation [75] was used

$$f_c(\theta) = 1 - e^{\frac{-0.5\Omega(\theta) LAI}{\cos(\theta)}}. \tag{12}$$

The UAV can help get maps of NDVI, LAI, $f_c(\theta)$, and $T_R(\theta)$, which are the most important input data for TSEB model. LE_c is initially estimated by using Priestley-Taylor formulation:

$$LE_c = \alpha_{PT} f_G \frac{\Delta}{\Delta + \gamma} R_{nc}, \tag{13}$$

where α_{PT} is the Priestley-Taylor coefficient. f_G is the LAI fraction. Δ is the slope of the saturation vapor pressure-temperature curve (Pa K^{-1}). γ is the psychrometric constant (Pa K^{-1}).

3.2. TSEB-PT model

In [27], the authors used two source energy balance models, the Priestley-Taylor TSEB (TSEB-PT) and the Dual-Temperature-Difference (DTD) when flying a fixed-wing UAV. The TSEB was first proposed by [76]. In 1995, Norman [26] applied an iterative process in order to derive the canopy and soil temperature. The method is based on the assumption of canopy transpiration, which was shown in Priestley and Taylor potential evapotranspiration [77]. Therefore, this method is called TSEB-PT in order to differentiate it from other TSEB methods. The TSEB-PT method splits the surface temperature into two layers, the canopy T_c and soil T_s temperatures. The calculation of sensible heat flux and latent

Preprints (www.preprints.org) | NOT PEER-REVIEWED | Posted: 8 July 2019 doi:10.20944/preprints201907.0124.v1

heat flux for canopy and soil are separate, which makes the parameterization of resistances easier compared with a single layer model.

3.3. Dual-Temperature-Difference DTD model

The DTD model was proposed in [78], which separates the land surface temperature into vegetation and soil temperatures. Then, it calculates the surface energy balance components with the same procedures as TSEB-PT. And, the DTD model can add one more input dataset, the land surface temperature retrieved one hour after sunrise. Because the energy fluxes are minimal at sunrise, it can help minimize the bias in the temperature estimation. In [79], Guzinski produced surface energy flux successfully by using the DTD model. The author used night observations to substitute for the early morning observation. However, the temporal resolution of the satellite observations is still limited, especially when the weather conditions are bad, such as overcast as satellite thermal infrared observations cannot penetrate clouds. The incapacity to collect data in overcast situations applies to all satellite sensors except for those operating in the microwaves region [79].

The calculation of soil heat flux G is also different because the radiometric temperature is dissimilar between midday and sunrise observations. This difference can be used to estimate the soil surface temperature variations. Soil heat flux is calculated based on the model of [80]. For more details about the TSEB-PT and DTD equations, see [81] [82].

By using the UAV platform, it can get better data in accordance with the DTD requirements and during overcast conditions [83].

3.4. METRIC model

METRIC is originally a satellite images processing model for estimating ET as a residual of the energy balance, which was developed by University of Idaho. METRIC has a self-calibration process which contains ground-based hourly reference ET and the selection of hot, cold pixels [84]. The METRIC is based on SEBAL. SEBAL's innovative component is that the model uses a near-surface temperature gradient, dT. It helps eliminating the need for absolute surface temperature calibration [11]. SEBAL uses Ts, ρ, NDVI and their relationships to calculate the surface fluxes [18]. And SEBAL has been evaluated all over the world [85] [86] [87] [88] [89]. In METRIC, they use the SEBAL to estimate dT. Therefore, there is no need to get accurate aerodynamic surface temperature. In [1], the author summarized three differences between the SEBAL and METRIC. First, for the cold pixel, the METRIC does not consider sensible heat flux as zero. Instead, a surface soil water balance is applied to set ET as zero and 1.05 times reference ET at hot and cold pixels respectively. Reference ET is calculated by using the standardized ASCE Penman-Monteith equation. Second, in METRIC, cold pixels are selected in agricultural settings instead of biophysical characteristics. Third, the extrapolation of instantaneous ET is based on reference ET instead of the actual evaporative fraction.

Allan [17] compared the ET estimation between the METRIC and lysimeter near the Montpelier, Idaho. The difference between METRIC and lysimter is only 4 %. LE is the rate of latent heat loss from the surface because of the ET. METRIC estimates ET as a residual of the energy balance

$$LE = R_n - G - H, \tag{14}$$

where R_n is the net radiation (W m^{-2}), which is calculated by solving the radiation balance as described in [90]. H is for sensible heat flux (W m^{-2}), which is a function of air density, air specific heat, temperature difference between two canopy heights, the aerodynamic resistance, and temperature gradient. LE is for latent heat flux (W m^{-2}) and G is for soil heat flux (W m^{-2}).

For the R_n, it can be calculated based on the following equation [25]:

$$R_n = (1 - \alpha)R_{s\downarrow} + R_{L\downarrow} - R_{L\uparrow} - (1 - \varepsilon_o)R_{L\downarrow}, \tag{15}$$

Preprints (www.preprints.org) | NOT PEER-REVIEWED | Posted: 8 July 2019 doi:10.20944/preprints201907.0124.v1

where $R_{s\downarrow}$ is the incoming short-wave radiation (W m^{-2}). α is the surface albedo, which is dimensionless. $R_{L\downarrow}$ and $R_{L\uparrow}$ are the incoming long-wave radiation (W m^{-2}) and outgoing long-wave radiation (W m^{-2}), respectively. ε_o is the thermal emissivity, which is also dimensionless.

$R_{s\downarrow}$ is usually calculated by the following equation if the sky is clear

$$R_{s\downarrow} = \frac{G_{sc} \cos \theta_{ref} \tau_{sw}}{d^2}, \tag{16}$$

where G_{sc} is the solar constant (1367 W m^{-2}). θ_{ref} is the solar incidence angle. d is the relative distance between the Earth and the Sun. τ_{sw} is the broad band atmospheric transmissivity, which is calculated by using the following equation [91]

$$\tau_{sw} = 0.35 + 0.627 \exp\left[\frac{-0.00146P}{K_t \cos \theta_{hor}} - 0.075\left(\frac{W}{\cos \theta_{hor}}\right)^{0.4}\right], \tag{17}$$

where P is the atmospheric pressure (kPa). W is the water in the atmosphere (mm). θ_{hor} is the solar zenith angle over a horizontal surface. K_t is the unitless turbidity coefficient. P and W are also calculated based on [91]

$$P = 101.3\left(\frac{293 - 0.0065z}{293}\right)^{5.26}, \tag{18}$$

$$W = 0.14 e_a P_{air} + 2.1, \tag{19}$$

where z is the elevation above the sea level. e_a is the near-surface vapor pressure (kPa).

For the incoming and outgoing long wave radiation $R_{L\downarrow}$ and $R_{L\uparrow}$, they are calculated by using Stefan-Boltzmann equation

$$R_{L\uparrow} = \varepsilon_o \sigma T_s^4, \tag{20}$$

$$R_{L\downarrow} = \varepsilon_a \sigma T_a^4, \tag{21}$$

where ε_a is effective atmospheric emissivity, which is usually calculated by an empirical equation

$$\varepsilon_a = 0.85(-\ln \tau_{sw})^{0..09}, \tag{22}$$

H is computed from surface roughness, wind speed, surface temperature ranges. The sensible heat flux is considered as the most difficult term to calculate in the energy balance equation, in order to calculate the H, an aerodynamic function is used:

$$H = \rho_{air} C_p \frac{dT}{r_{ah}}, \tag{23}$$

where r_{ah} is the aerodynamic resistance (s m^{-1}) between two surface height. In METRIC, r_{ah} is usually calculated by using the wind speed and an iterative stability correction, as shown in the following equation

$$r_{ah} = \frac{\ln(z_2/z_1)}{u_* k}, \tag{24}$$

where z_1 and z_2 are heights above the zero-plane displacement of the vegetation. k is the von Karman constant (0.41). u_* is the friction velocity (m s^{-1}), which is calculated by using

$$u_* = \frac{k u_{200}}{\ln(200/z_{om})}, \tag{25}$$

where u_{200} is the wind speed at a blending height 200m. And z_{om} is the momentum roughness length (m).

 doi:10.20944/preprints201907.0124.v1

dT is the temperature difference between the air and the surface. A strong linear relation between the dT and the surface temperature were found in [25] [18] [92] [93]. The equation for the dT and the surface temperature is shown as

$$dT = a + bT_s, \tag{26}$$

where a and b are derived parameters empirically based on two extreme hot and cold pixels. These hot and cold pixels defined the boundary of the sensible heat flux. The cold pixel represents a well-watered area with no water stress. The H is assumed to be minimum and ET should be maximum. The hot pixel represents a dry and bare field where H is maximum and ET is almost zero. Hot and cold pixels must be selected by experienced users, which makes it difficult for beginner level researchers.

In METRIC, G is the heat storage in soil and vegetation, which can be estimated by R_n surface temperature and vegetation index [85] according to

$$\frac{G}{R_n} = (T_s - 273.15)(0.0038 + 0.0074\alpha)(1 - 0.98NDVI^4). \tag{27}$$

Another equation used for estimating G is proposed by Tasumi [94], who used the data collected by [95].

$$\frac{G}{R_n} = 0.05 + 0.18e^{-0.521LAI}(LAI \geq 0.5), \tag{28}$$

$$\frac{G}{R_n} = 1.80\frac{(T_s - 273.15)}{R_n} + 0.084(LAI \leq 0.5). \tag{29}$$

Based on Tasumi's experiment results [94], the two above calculation methods can measure G accurately for irrigated plants in Kimberly, Idaho.

4. Results and Discussion

The comparison between UAV methods and results from other traditional remote sensing studies reveals that the data from the UAV platform and the light weight cameras can estimate the surface energy fluxes with similar accuracy estimated by using satellite data. Therefore, the UAV data can be used for modelling ET estimation with high confidence.

4.1. TSEB models

Mounted on the UAV, multispectral sensors and thermal camera can help obtain high-resolution images. In [37], the authors used a two-source energy balance model for a sub-field and plant canopy scale ET monitoring. It is concluded that the TSEB model can simulate the energy balance components in two vineyards with mean absolute error (MAE) ranging from 15 to 90 W m^{-2}. They found that the TSEB model is fairly robust and able to calculate LE and ET values under a varying environmental conditions. By using the TSEB, the T_s and T_c have a bias of 0.5 °C and RMSD on the order of 2.5 °C. The accuracy is similar with the following papers [96] [70] [69] [97] , in which the RMSD values are between 2.4 to 5.0 °C for T_s and 0.83 to 6.4 °C for T_c.

For a lightweight thermal camera mounted on a UAV, Hoffmann [27] concatenated the LST thermal images into orthomosaick, then applied as the input for TSEB model. Based on the comparison between UAV fluxes and eddy covariance (EC) fluxes, the R_n for TSEB is in good agreement with R_n measured from EC with a RMSE of 44 W m^{-2}. The sensible heat flux (H) for DTD has RMSE and MAE values of 59 W m^{-2} and 49 W m^{-2}. The soil heat flux (G) are underestimated, which has RMSE and MAE values of 48 W m^{-2} and 45 W m^{-2}. For the latent heat flux, DTD has RMSE and MAE values of 67 W m^{-2} and 57 W m^{-2}. They concluded that the TIR camera placed on a UAV platform can provide high spatial and temporal resolution data for estimating energy balance fluxes of ET. This study show similar results with Guzinski's work [81], who applied the TSEB-PT at the same site but used satellites

 doi:10.20944/preprints201907.0124.v1

images instead of UAV images. In [81], the RMSE is 46 W m^{-2} for R_n, 56 W m^{-2} for H, and 66 W m^{-2} for LE.

In [36], the RSEB algorithm was well implemented and only the climatic parameters, such as T_a, wind speed are measured as the input data. UAV images are used for calculating the NDVI and T_s. The authors evaluate the RSEB algorithm by H and LE. Results show that the algorithm estimates LE and H with errors of 7% and 5%. The RMSE and MAE for LE are 50 and 43 W m^{-2}. And, the RMSE and MAE for H are 56 and 46 W m^{-2}. It also concludes that high spatial resolution maps are capable to detect significant differences between the energy balance fluxes above the tree canopy and the soil surface between rows. UAV could also be used to help the satellite platforms for estimating spatial variability of ET maps.

4.2. SEBAL and METRIC models

In [68], Montibeller used multispectral and thermal camera to collect data for running the SEBAL model. To evaluate the estimated energy fluxes, they used linear regression models, residual plots, RMSE, and MAE methods. The R^2 for the R_n is 0.71, which was underestimated about 17% compared with the flux towers. The RMSE for the R_n is 6.09 W m^{-2}. For the G, the R^2 is 0.17, with a RMSE of 11.23 W m^{-2}. The R^2 for the H is 0.5, with a RMSE of 8.84 W m^{-2}. It overestimate the flux by 5 %. For the LE , R^2 is 0.82m, with a RMSE of 2.67 W m^{-2}. The research also shows that the ET rate is relevant to the crop growth stage. Corn, for example, has higher ET rates up until the tassel appears. However, the relationship between the NDVI and ET is very poor, further study need to be explored. Overall, the research proves that SEBAL model can be used for estimating ET with UAV very well. The algorithms being used by [68] were automated by Python, which facilitates the data processing foe ET estimation. This method can also be used for decision making in real time, which can monitor the waster consumption of each crop in the field.

5. Conclusions

According to the previous review, it shows that each ET estimation model has its own advantages and disadvantages. For example, METRIC/SEBAL methods, they are more recognized by the remote sensing researchers, but they are based on satellite (Landsat) platforms. It may require more efforts to make it work with UAV images. The TSEB model is less widely known, but it seems that it offers more potential for UAV applications in many crop conditions, for example, tree crops like pomegranate, nectarine, and almonds. When flying a drone, weather condition, field scale, flight time and many other factors should also be considered in order to choose the appropriate algorithms for ET estimation.

ET estimation methods and related agricultural applications have significantly been developing over the past decades. Although remote sensing ET models can help get relatively accurate spatial distribution ET data, important outstanding ET estimation questions are still from local to large scales because of the deficiency of our observation capability. No existing methods can fully satisfy the spatial, temporal, spectral, and accuracy requirements for ET-based science and applications [98]. Therefore, innovative methods or models for ET estimation are required by using UAVs. In [98], the author proposed five requirements to map ET with high fidelity in the future, which are high frequency, high spatial resolution, high temporal resolution, large spatial coverage, and long-term monitoring. High frequency will improve the differentiation of water stress between crops, which enables more efficient water management. High spatial resolution can help detect spatially heterogeneous responses to the water stress. Because ET is highly variable within and among days, high temporal resolution can help detect crops ET in real-time. Large spatial coverage can help detect large scale drought. And long term monitoring will be important to record ET variability.

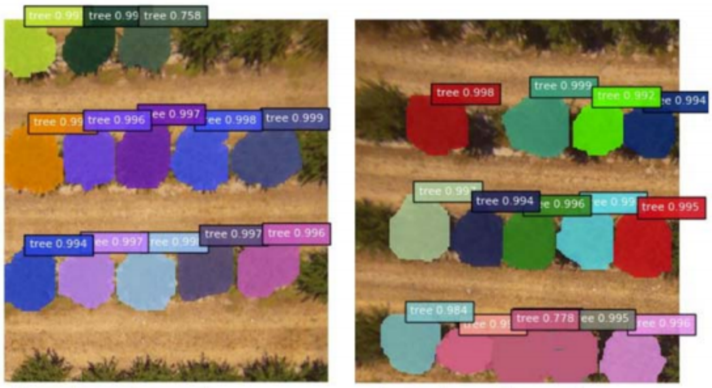

Figure 6. ET estimation in a single tree level

Compared with other satellites based remote sensing methods, UAV platform and light weight sensors can provide better quality, higher spatial and temporal resolution images. UAV can be used to estimate ET in excellent scale and with flexible flight schedules. In the future, tree-by-tree ET estimation would be useful to analyze the crops temporal and spatial variability in the field, as shown in Figure 6. In the [34], they used a deep learning neural network to train UAV images to identify tree canopies at very high accuracy, which have a great chance to be used in the future to estimate ET of a single tree. Also, further research should be focused on remote sensing algorithms and their applications on different crops.

Author Contributions: Haoyu Niu designed the experiments, processed and analyzed the UAV images, and wrote the original manuscript draft. Tiebiao Zhao, Dong Wang, and YangQuan Chen contributed to the results interpretation and discussions and editing of the manuscript.

Funding: This research is supported in part by USDA NIFA grant 2016-38422-25551 (2016-2020) entitled "Innovation and Entrepreneurship Programs to Train Hispanic Students for Future Agricultural and Food Industry".

Acknowledgments: Thanks go to Dong Sen Yan, Joshua Ahmed, Allan Murillo, Stella Zambrzuski and Christopher Currier for flying drones or collecting field measurements. We gratefully acknowledge the support of NVIDIA Corporation with the donation of the Titan X Pascal GPU used for this research.

Conflicts of Interest: The authors declare no conflict of interest.

Abbreviations

The following abbreviations are used in this manuscript:

MDPI	Multidisciplinary Digital Publishing Institute
ET	Evapotranspiration
UAV	Unmanned Aerial Vehicles
METRIC	Mapping Evapotranspiration at high Resolution with Internalized Calibration
NDVI	Normalized Difference Vegetation Index
SEBAL	Surface Energy Balance Algorithm for Land
RGB	Red Green and Blue
RSEB	Remote sensing energy balance
TSEB	Two source energy balance
TIR	Thermal infrared
FOV	Field of View
NIR	Near infrared
JPEG	Joint Photographic Experts Group
SWIR	Short-wave infrared
MAE	Mean absolute error

 doi:10.20944/preprints201907.0124.v1

Appendix A MATLAB code and Photoscan settings

Appendix A.1 Matlab code for calculating drone image NDVI

The Matlab code is attached here for calculating NDVI of drone images, which can be found at Github: https://github.com/niuhaoyu16/NDVI-for-drone-images

Appendix A.2 Agisoft Photoscan image processing settings

Agisoft Photoscan image processing settings is available at Github: https://github.com/niuhaoyu16/AgisoftPhotoscan-Images-processing-settings

Appendix B Open source python code for METRIC and TSEB

Appendix B.1 Python code for TSEB

PyTSEB is available at Github: https://github.com/hectornieto/pyTSEB

Appendix B.2 Python code for METRIC

PyMETRIC is available at Github: https://github.com/hectornieto/pyMETRIC

References

1. Liou, Y.A.; Kar, S. Evapotranspiration estimation with remote sensing and various surface energy balance algorithms—A review. *Energies* **2014**, *7*, 2821–2849.
2. Verstraeten, W.; Veroustraete, F.; Feyen, J. Assessment of evapotranspiration and soil moisture content across different scales of observation. *Sensors* **2008**, *8*, 70–117.
3. Eden, U. *Drought assessment by evapotranspiration mapping in Twente, the Netherlands*; University of Twente Faculty of Geo-Information and Earth Observation (ITC), 2012.
4. Kaplan, S.; Myint, S.W.; Fan, C.; Brazel, A.J. Quantifying outdoor water consumption of urban land use/land cover: sensitivity to drought. *Environmental management* **2014**, *53*, 855–864.
5. Wetzel, P.J.; Chang, J.T. Evapotranspiration from nonuniform surfaces: A first approach for short-term numerical weather prediction. *Monthly Weather Review* **1988**, *116*, 600–621.
6. Allen, R.G.; Pereira, L.S.; Raes, D.; Smith, M. FAO Irrigation and drainage paper No. 56. *Rome: Food and Agriculture Organization of the United Nations* **1998**, *56*, e156.
7. Liu, C.; Zhang, X.; Zhang, Y. Determination of daily evaporation and evapotranspiration of winter wheat and maize by large-scale weighing lysimeter and micro-lysimeter. *Agricultural and Forest Meteorology* **2002**, *111*, 109–120.
8. Xu, C.Y.; Singh, V. Evaluation of three complementary relationship evapotranspiration models by water balance approach to estimate actual regional evapotranspiration in different climatic regions. *Journal of Hydrology* **2005**, *308*, 105–121.
9. Idso, S.B.; Jackson, R.D.; Reginato, R.J. Estimating evaporation: a technique adaptable to remote sensing. *Science* **1975**, *189*, 991–992.
10. Grismer, M.E.; Orang, M.; Snyder, R.; Matyac, R. Pan evaporation to reference evapotranspiration conversion methods. *Journal of irrigation and drainage engineering* **2002**, *128*, 180–184.
11. Allen, R.; Irmak, A.; Trezza, R.; Hendrickx, J.M.; Bastiaanssen, W.; Kjaersgaard, J. Satellite-based ET estimation in agriculture using SEBAL and METRIC. *Hydrological Processes* **2011**, *25*, 4011–4027.
12. Angus, D.; Watts, P. Evapotranspiration-How good is the Bowen ratio method? In *Developments in Agricultural and Managed Forest Ecology*; Elsevier, 1984; Vol. 13, pp. 133–150.
13. Fritschen, L.J. Accuracy of evapotranspiration determinations by the Bowen ratio method. *Hydrological Sciences Journal* **1965**, *10*, 38–48.
14. Nagler, P.L.; Scott, R.L.; Westenburg, C.; Cleverly, J.R.; Glenn, E.P.; Huete, A.R. Evapotranspiration on western US rivers estimated using the Enhanced Vegetation Index from MODIS and data from eddy covariance and Bowen ratio flux towers. *Remote sensing of environment* **2005**, *97*, 337–351.

15. Su, Z. The Surface Energy Balance System (SEBS) for estimation of turbulent heat fluxes. *Hydrology and earth system sciences* **2002**, *6*, 85–100.
16. Kustas, W.; Anderson, M. Advances in thermal infrared remote sensing for land surface modeling. *Agricultural and Forest Meteorology* **2009**, *149*, 2071–2081.
17. Allen, R.G.; Tasumi, M.; Morse, A.; Trezza, R. A Landsat-based energy balance and evapotranspiration model in Western US water rights regulation and planning. *Irrigation and Drainage systems* **2005**, *19*, 251–268.
18. Bastiaanssen, W.G.; Pelgrum, H.; Wang, J.; Ma, Y.; Moreno, J.; Roerink, G.; Van der Wal, T. A remote sensing surface energy balance algorithm for land (SEBAL).: Part 2: Validation. *Journal of hydrology* **1998**, *212*, 213–229.
19. Bastiaanssen, W.G.; Menenti, M.; Feddes, R.; Holtslag, A. A remote sensing surface energy balance algorithm for land (SEBAL). 1. Formulation. *Journal of hydrology* **1998**, *212*, 198–212.
20. Kustas, W.P.; Norman, J.M. A two-source approach for estimating turbulent fluxes using multiple angle thermal infrared observations. *Water Resources Research* **1997**, *33*, 1495–1508.
21. Park, S. Estimating plant water stress and evapotranspiration using very-high-resolution (VHR) UAV imagery. PhD thesis, 2018.
22. Quattrochi, D.A.; Luvall, J.C. Thermal infrared remote sensing for analysis of landscape ecological processes: methods and applications. *Landscape ecology* **1999**, *14*, 577–598.
23. Moran, M.S.; Jackson, R.D. Assessing the spatial distribution of evapotranspiration using remotely sensed inputs. *Journal of Environmental Quality* **1991**, *20*, 725–737.
24. Kustas, W.; Norman, J. Use of remote sensing for evapotranspiration monitoring over land surfaces. *Hydrological Sciences Journal* **1996**, *41*, 495–516.
25. Allen, R.G.; Tasumi, M.; Trezza, R. Satellite-based energy balance for mapping evapotranspiration with internalized calibration (METRIC)—Model. *Journal of irrigation and drainage engineering* **2007**, *133*, 380–394.
26. Norman, J.M.; Kustas, W.P.; Humes, K.S. Source approach for estimating soil and vegetation energy fluxes in observations of directional radiometric surface temperature. *Agricultural and Forest Meteorology* **1995**, *77*, 263–293.
27. Hoffmann, H.; Nieto, H.; Jensen, R.; Guzinski, R.; Zarco-Tejada, P.; Friborg, T. Estimating evaporation with thermal UAV data and two-source energy balance models. *Hydrology and Earth System Sciences* **2016**, *20*, 697–713.
28. Cammalleri, C.; Anderson, M.; Gao, F.; Hain, C.; Kustas, W. A data fusion approach for mapping daily evapotranspiration at field scale. *Water Resources Research* **2013**, *49*, 4672–4686.
29. Díaz-Varela, R.; de la Rosa, R.; León, L.; Zarco-Tejada, P. High-resolution airborne UAV imagery to assess olive tree crown parameters using 3D photo reconstruction: application in breeding trials. *Remote Sensing* **2015**, *7*, 4213–4232.
30. Gonzalez-Dugo, V.; Goldhamer, D.; Zarco-Tejada, P.J.; Fereres, E. Improving the precision of irrigation in a pistachio farm using an unmanned airborne thermal system. *Irrigation science* **2015**, *33*, 43–52.
31. Swain, K.C.; Thomson, S.J.; Jayasuriya, H.P. Adoption of an unmanned helicopter for low-altitude remote sensing to estimate yield and total biomass of a rice crop. *Transactions of the ASABE* **2010**, *53*, 21–27.
32. Zarco-Tejada, P.J.; González-Dugo, V.; Williams, L.; Suárez, L.; Berni, J.A.; Goldhamer, D.; Fereres, E. A PRI-based water stress index combining structural and chlorophyll effects: Assessment using diurnal narrow-band airborne imagery and the CWSI thermal index. *Remote sensing of environment* **2013**, *138*, 38–50.
33. Zhao, T.; Chen, Y.; Ray, A.; Doll, D. Quantifying almond water stress using unmanned aerial vehicles (uavs): correlation of stem water potential and higher order moments of non-normalized canopy distribution. ASME 2017 International Design Engineering Technical Conferences and Computers and Information in Engineering Conference. American Society of Mechanical Engineers, 2017, pp. V009T07A058–V009T07A058.
34. Zhao, T.; Niu, H.; de la Rosa, E.; Doll, D.; Wang, D.; Chen, Y. Tree canopy differentiation using instance-aware semantic segmentation. 2018 ASABE Annual International Meeting. American Society of Agricultural and Biological Engineers, 2018, p. 1.
35. Zhao, T.; Wang, Z.; Yang, Q.; Chen, Y. Melon yield prediction using small unmanned aerial vehicles. Autonomous Air and Ground Sensing Systems for Agricultural Optimization and Phenotyping II. International Society for Optics and Photonics, 2017, Vol. 10218, p. 1021808.

 doi:10.20944/preprints201907.0124.v1

36. Ortega-Farías, S.; Ortega-Salazar, S.; Poblete, T.; Kilic, A.; Allen, R.; Poblete-Echeverría, C.; Ahumada-Orellana, L.; Zuñiga, M.; Sepúlveda, D. Estimation of energy balance components over a drip-irrigated olive orchard using thermal and multispectral cameras placed on a helicopter-based unmanned aerial vehicle (UAV). *Remote Sensing* **2016**, *8*, 638.
37. Xia, T.; Kustas, W.P.; Anderson, M.C.; Alfieri, J.G.; Gao, F.; McKee, L.; Prueger, J.H.; Geli, H.M.; Neale, C.M.; Sanchez, L.; others. Mapping evapotranspiration with high-resolution aircraft imagery over vineyards using one-and two-source modeling schemes. *Hydrology and Earth System Sciences* **2016**, *20*, 1523.
38. Zhao, T.; Yang, Y.; Niu, H.; Wang, D.; Chen, Y. Comparing U-Net convolutional network with mask R-CNN in the performances of pomegranate tree canopy segmentation. Multispectral, Hyperspectral, and Ultraspectral Remote Sensing Technology, Techniques and Applications VII. International Society for Optics and Photonics, 2018, Vol. 10780, p. 107801J.
39. Brown, K.; Rosenberg, N.J. A Resistance Model to Predict Evapotranspiration and Its Application to a Sugar Beet Field 1. *Agronomy Journal* **1973**, *65*, 341–347.
40. Elarab, M. The application of unmanned aerial vehicle to precision agriculture: Chlorophyll, nitrogen, and evapotranspiration estimation **2016**.
41. Sheng, H.; Chao, H.; Coopmans, C.; Han, J.; McKee, M.; Chen, Y. Low-cost UAV-based thermal infrared remote sensing: Platform, calibration and applications. Mechatronics and Embedded Systems and Applications (MESA), 2010 IEEE/ASME International Conference on. IEEE, 2010, pp. 38–43.
42. Ribeiro-Gomes, K.; Hernández-López, D.; Ortega, J.F.; Ballesteros, R.; Poblete, T.; Moreno, M.A. Uncooled Thermal Camera Calibration and Optimization of the Photogrammetry Process for UAV Applications in Agriculture. *Sensors* **2017**, *17*, 2173.
43. Berni, J.A.; Zarco-Tejada, P.J.; Suárez, L.; Fereres, E. Thermal and narrowband multispectral remote sensing for vegetation monitoring from an unmanned aerial vehicle. *IEEE Transactions on Geoscience and Remote Sensing* **2009**, *47*, 722–738.
44. Gade, R.; Moeslund, T.B. Thermal cameras and applications: a survey. *Machine vision and applications* **2014**, *25*, 245–262.
45. Martinelli, F.; Scalenghe, R.; Davino, S.; Panno, S.; Scuderi, G.; Ruisi, P.; Villa, P.; Stroppiana, D.; Boschetti, M.; Goulart, L.R.; others. Advanced methods of plant disease detection. A review. *Agronomy for Sustainable Development* **2015**, *35*, 1–25.
46. Zhao, T.; Stark, B.; Chen, Y.; Ray, A.; Doll, D. More reliable crop water stress quantification using small unmanned aerial systems (suas). *IFAC-PapersOnLine* **2016**, *49*, 409–414.
47. Zhao, T.; Stark, B.; Chen, Y.; Ray, A.L.; Doll, D. A detailed field study of direct correlations between ground truth crop water stress and normalized difference vegetation index (ndvi) from small unmanned aerial system (suas). 2015 International Conference on Unmanned Aircraft Systems (ICUAS). IEEE, 2015, pp. 520–525.
48. Soliman, A.; Heck, R.J.; Brenning, A.; Brown, R.; Miller, S. Remote sensing of soil moisture in vineyards using airborne and ground-based thermal inertia data. *Remote Sensing* **2013**, *5*, 3729–3748.
49. Jones, H.G.; Serraj, R.; Loveys, B.R.; Xiong, L.; Wheaton, A.; Price, A.H. Thermal infrared imaging of crop canopies for the remote diagnosis and quantification of plant responses to water stress in the field. *Functional Plant Biology* **2009**, *36*, 978–989.
50. Gowen, A.; Tiwari, B.; Cullen, P.; McDonnell, K.; O'Donnell, C. Applications of thermal imaging in food quality and safety assessment. *Trends in food science & technology* **2010**, *21*, 190–200.
51. Zhao, T.; Niu, H.; Anderson, A.; Chen, Y.; Viers, J. A detailed study on accuracy of uncooled thermal cameras by exploring the data collection workflow. Autonomous Air and Ground Sensing Systems for Agricultural Optimization and Phenotyping III. International Society for Optics and Photonics, 2018, Vol. 10664, p. 106640F.
52. Näsi, R.; Honkavaara, E.; Lyytikäinen-Saarenmaa, P.; Blomqvist, M.; Litkey, P.; Hakala, T.; Viljanen, N.; Kantola, T.; Tanhuanpää, T.; Holopainen, M. Using UAV-based photogrammetry and hyperspectral imaging for mapping bark beetle damage at tree-level. *Remote Sensing* **2015**, *7*, 15467–15493.
53. Stark, B.; Chen, Y. A framework of optimal remote sensing using small unmanned aircraft systems. 2016 12th IEEE/ASME International Conference on Mechatronic and Embedded Systems and Applications (MESA). IEEE, 2016, pp. 1–6.

54. Harwin, S.; Lucieer, A. Assessing the accuracy of georeferenced point clouds produced via multi-view stereopsis from unmanned aerial vehicle (UAV) imagery. *Remote Sensing* **2012**, *4*, 1573–1599.
55. Lucieer, A.; Malenovskỳ, Z.; Veness, T.; Wallace, L. HyperUAS—Imaging spectroscopy from a multirotor unmanned aircraft system. *Journal of Field Robotics* **2014**, *31*, 571–590.
56. Turner, D.; Lucieer, A.; Watson, C. An automated technique for generating georectified mosaics from ultra-high resolution unmanned aerial vehicle (UAV) imagery, based on structure from motion (SfM) point clouds. *Remote sensing* **2012**, *4*, 1392–1410.
57. Wallace, L.; Lucieer, A.; Watson, C.; Turner, D. Development of a UAV-LiDAR system with application to forest inventory. *Remote Sensing* **2012**, *4*, 1519–1543.
58. Smith, G.M.; Milton, E.J. The use of the empirical line method to calibrate remotely sensed data to reflectance. *International Journal of remote sensing* **1999**, *20*, 2653–2662.
59. Kamble, B.; Kilic, A.; Hubbard, K. Estimating crop coefficients using remote sensing-based vegetation index. *Remote sensing* **2013**, *5*, 1588–1602.
60. Reyes-Gonzalez, A.; Hay, C.; Kjaersgaard, J.; Neale, C. Use of remote sensing to generate crop coefficient and estimate actual crop evapotranspiration. 2015 ASABE Annual International Meeting. American Society of Agricultural and Biological Engineers, 2015, p. 1.
61. Hunsaker, D.J.; Pinter, P.J.; Barnes, E.M.; Kimball, B.A. Estimating cotton evapotranspiration crop coefficients with a multispectral vegetation index. *Irrigation science* **2003**, *22*, 95–104.
62. Jackson, R.; Reginato, R.; Idso, S. Wheat canopy temperature: a practical tool for evaluating water requirements. *Water resources research* **1977**, *13*, 651–656.
63. SEGUIN, B.; ITIER, B. Using midday surface temperature to estimate daily evaporation from satellite thermal IR data. *International Journal of Remote Sensing* **1983**, *4*, 371–383.
64. Moran, M.; Clarke, T.; Inoue, Y.; Vidal, A. Estimating crop water deficit using the relation between surface-air temperature and spectral vegetation index. *Remote sensing of environment* **1994**, *49*, 246–263.
65. Carlson, T.N.; Gillies, R.R.; Schmugge, T.J. An interpretation of methodologies for indirect measurement of soil water content. *Agricultural and forest meteorology* **1995**, *77*, 191–205.
66. Anderson, M.; Neale, C.; Li, F.; Norman, J.; Kustas, W.; Jayanthi, H.; Chavez, J. Upscaling ground observations of vegetation water content, canopy height, and leaf area index during SMEX02 using aircraft and Landsat imagery. *Remote sensing of environment* **2004**, *92*, 447–464.
67. Carlson, T.N.; Ripley, D.A. On the relation between NDVI, fractional vegetation cover, and leaf area index. *Remote sensing of Environment* **1997**, *62*, 241–252.
68. Montibeller, Á.G. Estimating energy fluxes and evapotranspiration of corn and soybean with an unmanned aircraft system in Ames, Iowa **2017**.
69. Kustas, W.P.; Norman, J.M. Evaluation of soil and vegetation heat flux predictions using a simple two-source model with radiometric temperatures for partial canopy cover. *Agricultural and Forest Meteorology* **1999**, *94*, 13–29.
70. Kustas, W.P.; Norman, J.M. A two-source energy balance approach using directional radiometric temperature observations for sparse canopy covered surfaces. *Agronomy Journal* **2000**, *92*, 847–854.
71. French, A.N.; Hunsaker, D.J.; Thorp, K.R. Remote sensing of evapotranspiration over cotton using the TSEB and METRIC energy balance models. *Remote Sensing of Environment* **2015**, *158*, 281–294.
72. Choi, M.; Kustas, W.P.; Anderson, M.C.; Allen, R.G.; Li, F.; Kjaersgaard, J.H. An intercomparison of three remote sensing-based surface energy balance algorithms over a corn and soybean production region (Iowa, US) during SMACEX. *Agricultural and Forest Meteorology* **2009**, *149*, 2082–2097.
73. Colaizzi, P.; Evett, S.; Howell, T.; Li, F.; Kustas, W.; Anderson, M. Radiation model for row crops: I. Geometric view factors and parameter optimization. *Agronomy journal* **2012**, *104*, 225–240.
74. Song, L.; Liu, S.; Kustas, W.P.; Zhou, J.; Xu, Z.; Xia, T.; Li, M. Application of remote sensing-based two-source energy balance model for mapping field surface fluxes with composite and component surface temperatures. *Agricultural and forest meteorology* **2016**, *230*, 8–19.
75. Campbell, G.S.; Norman, J.M. *An introduction to environmental biophysics*; Springer Science & Business Media, 2012.
76. Shuttleworth, W.J.; Wallace, J. Evaporation from sparse crops-an energy combination theory. *Quarterly Journal of the Royal Meteorological Society* **1985**, *111*, 839–855.

77. Priestley, C.H.B.; Taylor, R. On the assessment of surface heat flux and evaporation using large-scale parameters. *Monthly weather review* **1972**, *100*, 81–92.
78. Norman, J.; Kustas, W.; Prueger, J.; Diak, G. Surface flux estimation using radiometric temperature: A dual-temperature-difference method to minimize measurement errors. *Water Resources Research* **2000**, *36*, 2263–2274.
79. Guzinski, R.; Anderson, M.C.; Kustas, W.P.; Nieto, H.; Sandholt, I. Using a thermal-based two source energy balance model with time-differencing to estimate surface energy fluxes with day-night MODIS observations. *Hydrology and Earth System Sciences* **2013**, *17*, 2809–2825.
80. Santanello Jr, J.A.; Friedl, M.A. Diurnal covariation in soil heat flux and net radiation. *Journal of Applied Meteorology* **2003**, *42*, 851–862.
81. Guzinski, R.; Nieto, H.; Jensen, R.; Mendiguren, G. Remotely sensed land-surface energy fluxes at sub-field scale in heterogeneous agricultural landscape and coniferous plantation. *Biogeosciences* **2014**, *11*, 5021–5046.
82. Guzinski, R.; Nieto, H.; Stisen, S.; Fensholt, R. Inter-comparison of energy balance and hydrological models for land surface energy flux estimation over a whole river catchment. *Hydrology and Earth System Sciences* **2015**, *19*, 2017–2036.
83. Hunt, E.R.; Cavigelli, M.; Daughtry, C.S.; Mcmurtrey, J.E.; Walthall, C.L. Evaluation of digital photography from model aircraft for remote sensing of crop biomass and nitrogen status. *Precision Agriculture* **2005**, *6*, 359–378.
84. Gowda, P.H.; Chavez, J.L.; Colaizzi, P.D.; Evett, S.R.; Howell, T.A.; Tolk, J.A. ET mapping for agricultural water management: present status and challenges. *Irrigation science* **2008**, *26*, 223–237.
85. Bastiaanssen, W.G. SEBAL-based sensible and latent heat fluxes in the irrigated Gediz Basin, Turkey. *Journal of hydrology* **2000**, *229*, 87–100.
86. Bastiaanssen, W.G.; Ahmad, M.u.D.; Chemin, Y. Satellite surveillance of evaporative depletion across the Indus Basin. *Water Resources Research* **2002**, *38*, 9–1.
87. Ruhoff, A.L.; Paz, A.R.; Collischonn, W.; Aragao, L.E.; Rocha, H.R.; Malhi, Y.S. A MODIS-based energy balance to estimate evapotranspiration for clear-sky days in Brazilian tropical savannas. *Remote Sensing* **2012**, *4*, 703–725.
88. Singh, R.; Senay, G. Comparison of four different energy balance models for estimating evapotranspiration in the Midwestern United States. *Water* **2016**, *8*, 9.
89. Sun, Z.; Wei, B.; Su, W.; Shen, W.; Wang, C.; You, D.; Liu, Z. Evapotranspiration estimation based on the SEBAL model in the Nansi Lake Wetland of China. *Mathematical and Computer Modelling* **2011**, *54*, 1086–1092.
90. Allen, R.; Tasumi, M.; Trezza, R.; Kjaersgaard, J. METRICTM–Mapping Evapotranspiration at high resolution–Applications Manual for Landsat Satellite Imagery (Version 2.0. 4). *University of Idaho* **2008**.
91. Walter, I.A.; Allen, R.G.; Elliott, R.; Jensen, M.; Itenfisu, D.; Mecham, B.; Howell, T.; Snyder, R.; Brown, P.; Echings, S.; others. ASCE's standardized reference evapotranspiration equation. In *Watershed management and operations management 2000*; 2000; pp. 1–11.
92. Bastiaanssen, W.; Noordman, E.; Pelgrum, H.; Davids, G.; Thoreson, B.; Allen, R. SEBAL model with remotely sensed data to improve water-resources management under actual field conditions. *Journal of irrigation and drainage engineering* **2005**, *131*, 85–93.
93. Jacob, F.; Olioso, A.; Gu, X.F.; Su, Z.; Seguin, B. Mapping surface fluxes using airborne visible, near infrared, thermal infrared remote sensing data and a spatialized surface energy balance model. *Agronomie* **2002**, *22*, 669–680.
94. Tasumi, M. Progress in operational estimation of regional evapotranspiration using satellite imagery. **2004**.
95. Wright, J.L. New evapotranspiration crop coefficients. *Proceedings of the American Society of Civil Engineers, Journal of the Irrigation and Drainage Division* **1982**, *108*, 57–74.
96. Li, F.; Kustas, W.P.; Prueger, J.H.; Neale, C.M.; Jackson, T.J. Utility of remote sensing–based two-source energy balance model under low-and high-vegetation cover conditions. *Journal of Hydrometeorology* **2005**, *6*, 878–891.
97. Colaizzi, P.D.; Kustas, W.P.; Anderson, M.C.; Agam, N.; Tolk, J.A.; Evett, S.R.; Howell, T.A.; Gowda, P.H.; O'Shaughnessy, S.A. Two-source energy balance model estimates of evapotranspiration using component and composite surface temperatures. *Advances in water resources* **2012**, *50*, 134–151.

 doi:10.20944/preprints201907.0124.v1

98. Fisher, J.B.; Melton, F.; Middleton, E.; Hain, C.; Anderson, M.; Allen, R.; McCabe, M.F.; Hook, S.; Baldocchi, D.; Townsend, P.A.; others. The future of evapotranspiration: Global requirements for ecosystem functioning, carbon and climate feedbacks, agricultural management, and water resources. *Water Resources Research* **2017**, *53*, 2618–2626.